Published version has doi: 10.1016/j.gloplacha.2019.103084.

An experiment to test satellite radar interferometry-observed geodetic ties to remotely monitor vertical land motion at tide gauges

M.S. Filmer[1], S.P.D. Williams[2], C.W. Hughes[2,3], G. Wöppelmann[4], W.E. Featherstone[1], P.L. Woodworth[2], A.L. Parker[1,5]

1. School of Earth and Planetary Sciences, Curtin University, GPO Box U1987, Perth, WA 6845, Australia
2. National Oceanography Centre, Joseph Proudman Building, 6 Brownlow Street, Liverpool, L3 5DA, UK
3. School of Environmental Sciences, University of Liverpool, Liverpool, L69 3GP, UK
4. Littoral, Environment and Societies (LIENS), University of La Rochelle – National Centre for Scientific Research (CNRS), 2 rue Olympe de Gouges, 17000 La Rochelle, France
5. Commonwealth Scientific and Industrial Research Organisation (CSIRO), 26 Dick Perry Drive, Kensington, WA 6103, Australia

Corresponding author: M.Filmer@curtin.edu.au

ORCIDs

M.S. Filmer: http://orcid.org/0000-0002-3555-4869
S.P.D. Williams: http://orcid.org/0000-0003-4123-4973
C.W. Hughes: http://orcid.org/0000-0002-9355-0233
G. Wöppelmann: http://orcid.org/0000-0001-7178-2503
W.E. Featherstone: http://orcid.org/0000-0001-9644-4535
P.L. Woodworth: http://orcid.org/0000-0002-6681-239X
A.L. Parker: http://orcid.org/0000-0003-4342-9301

Highlights:

- Differential InSAR can provide vertical land motion estimates at tide gauges.
- Differential InSAR and tide gauge minus altimetry agree for adjacent tide gauges.

- Possible systematic offset in absolute trends from tide gauge minus altimetry.
- Comparison of 20- and 5-year trends suggest non-linear vertical tide gauge motion.

Abstract: The nature and linearity of vertical land motion (VLM) impacting the global sea level record from tide gauges is not well known, but remains of importance to understand long-term changes to sea level. Local surveys are required to directly measure VLM at tide gauges relative to a global reference frame, but this is limited by the lack of differential VLM measurements between tide gauges and continuously operating GPS (cGPS) stations that are not co-located, i.e., fixed to the tide gauge structure. We present results from an experiment using satellite radar interferometry (InSAR) scenes acquired from the TerraSAR-X satellite mission to test whether InSAR could replace repeat geodetic levelling as a 'geodetic tie' between cGPS stations and tide gauges. Comparisons are made among TerraSAR-X, cGPS and tide gauge minus altimetry VLM estimates for the Hillarys and Fremantle tide gauges (Perth, Western Australia), which are used as test sites for this method. The results suggest agreement between differential TerraSAR-X and altimetry minus tide gauge VLM rates, but systematic offsets among the absolute/geocentric rates. The TerraSAR-X VLM at the Fremantle tide gauge for the period 7 October 2012 – 7 October 2017 is +0.45±0.40 mm/yr (referenced to IGS08 at PERT cGPS), although this should be treated cautiously over this short period, and also that VLM at Fremantle and Hillarys appear to be non-linear over time. We infer from this that the uncertainties in TerraSAR-X differential VLM rates are comparable to those from the highest quality repeat levelling.

Key words: InSAR, sea level change, vertical land motion, tide gauges

1. Introduction

Estimates of sea level change (SLC) rates and their de/acceleration determined by tide gauges fixed to the Earth's surface are susceptible to vertical land motion (VLM), i.e., subsidence or

uplift, at their locations. Studies have focussed on these effects on global (e.g., Wöppelmann and Marcos 2016; Hamlington et al. 2016; Santamaría-Gómez et al. 2017) and local (e.g., Raucoules et al. 2013; Wöppelmann et al. 2013; Featherstone et al. 2015; Bekaert et al. 2017; Poitevin et al. 2019) scales. Tide gauges undergoing subsidence will imply an inflated rate of sea level rise, and those experiencing uplift will show a lower rate of sea level rise, and potentially sea level fall if the uplift is larger than the magnitude of long-term sea level rise, such as in Fennoscandia and northern North America (e.g., Mazzotti et al. 2008). An additional complexity is that non-linear VLM may imply artificial acceleration or deceleration, or simply mask any real change in the linear rate of SLC.

Tide gauge VLM can be caused by anthropogenic effects due to groundwater/fluid/gas extraction (e.g., Fielding et al. 1998; Brooks et al. 2007; Raucoules et al. 2013) or natural variation at regional scale due to tectonics, glacial isostatic adjustment (GIA), or a combination of some or all (e.g., Wöppelmann and Marcos 2016). Various methods have been used to estimate tide gauge VLM, including the use of continuous GPS (cGPS) stations at or near tide gauges (Bevis et al. 2002), GIA models (Peltier 2004), and subtraction of satellite altimetry measurements of the sea surface adjacent to the tide gauge from the sea level recorded by the tide gauge (Kuo et al. 2004). In the latter, the difference is taken to be VLM at the tide gauge, on the assumption that the altimetry and tide gauge sea level records should be observing the same sea level rate in the absence of any artefacts (Wöppelmann and Marcos, 2016).

While all of these methods provide estimates of tide gauge VLM, they have limitations, either in their measurement and processing, or that they may not be directly measuring VLM at the tide gauge. For example, cGPS may be placed near tide gauges, but still a kilometre or more away (e.g., King et al. 2012), so that local differential VLM between the cGPS station and the tide gauge will mean that the VLM rate from the cGPS time series

may be different to the actual rate at the tide gauge (e.g., Featherstone et al. 2015). The conventional method of monitoring differential VLM between the tide gauge and cGPS station is by repeat differential levelling, which as a quality control for first order usually has a maximum allowable misclosure of $2\sqrt{d}$ mm (d is the one way distance between levelling endpoints in km) for two-way levelling forward and reverse between benchmarks. Note, though, that levelling measures differential VLM relative to a geopotential surface. When the geopotential is also changing, this can differ from the purely geometric definitions of VLM from other techniques. In general, it is expected that these differences will be negligible over a few kms compared to the differential VLM itself.

An example of the precision of high quality levelling is Lyon et al. (2018), who used an east-west repeat levelling traverse across the Perth Basin to demonstrate that when best practice in field and processing procedures are followed, a misclosure precision of ~$0.45\sqrt{d}$ mm can be achieved. This standard of levelling was shown to achieve rate uncertainties of between ±0.10 mm/yr and ±1.87 mm/yr over four years for a 65-benchmark ~40 km long repeat levelling line. The median for these uncertainties is ±0.44 mm/yr, which could be considered a best case precision over a ~4 year levelling time series, with two repeat surveys conducted each year. Woodworth et al. (2017) refer to a repeat levelling connection as a 'geodetic tie', however, this connection is often not done by the agencies usually tasked with the surveys, usually due to funding/resource constraints and the perceived low priority placed on these ties.

A feasible alternative to determine differential VLM between tide gauges and cGPS stations is shown here through the use of satellite-borne InSAR (interferometric synthetic aperture radar), and more specifically, methods such as persistent scatterer interferometry (PSI) (e.g., Feretti et al. 2000; Kampes 2006; Hooper et al. 2007), and/or small baseline multi-temporal InSAR (MTI; Hooper 2008; Hooper et al 2012). InSAR has been

demonstrated to estimate line of sight (LoS to satellite) land displacement at 1 mm/yr precision, or in some circumstances less, depending on the number of SAR scenes and length of the time series (e.g., Rucci et al. 2012; Cao et al. 2018). There have been a number of InSAR studies that have investigated coastal VLM, including near tide gauges, e.g., Brooks et al. (2007) in the Los Angeles area, Adamska (2012) at tide gauges in the UK, Raucoules et al. (2013) in Manilla, the Philippines, Wöppelmann et al. (2013) in Alexandria, Egypt, Le Cozannet et al. (2014; 2015) in Dakar, Senegal, Bekaert et al. (2017) in the Chesapeake Bay region of the USA, and Poitevin et al. (2019) at Brest, France. All of these have used InSAR to estimate VLM in the coastal area surrounding the tide gauge(s), inferring VLM at the tide gauge. However, they have not used them as a dedicated geodetic tie between a cGPS and the tide gauge, as we propose and test here.

We describe experiments using five integer years of SAR acquisitions from the German Aerospace Agency's (DLR's) TerraSAR-X (TSX) satellite mission over a test site containing the Fremantle (FREM) and Hillarys (HILS) tide gauges in Perth (Australia). These tide gauges are suitable for this experiment because (1) HILS has a co-located cGPS (fixed to the tide gauges structure) that can be used for validation, (2) FREM has a long running (>100 year) tide gauge record, and (3) the tide gauges are ~30 km apart, so can be used to test the differential VLM between them. HILS is known to be undergoing non-linear VLM (Featherstone et al. 2015), while Featherstone et al. (2015) has suggested FREM is also undergoing non-linear VLM (cf. Thompson and Merrifield 2018; Burgette et al. 2013).

Other SAR scenes are available over the test site, e.g., C-band scenes from the European Space Agency's Envisat and Sentinel-1 satellite missions, but neither provide a sufficiently long time series nor the number of scenes that we have available from TSX. For example, Sentinel-1A started acquisitions in 2014 and observed the test site for an eight month period (e.g., Parker et al. 2017a), while Sentinel-1B did not begin observations until

2016. Comparisons between X-band and C-band displacements in Parker et al. (2017a) indicated reasonable agreement between these data although over a very short period, so not conclusive. Using 141 TSX scenes acquired between 7 October 2012 and 7 October 2017 (herein referred to by decimal years 2012.8-2017.8 to denote five integer years), we have estimated VLM rates at these tide gauges in the test site to determine the utility of InSAR to monitor differential VLM between tide gauges and cGPS stations as an alternative to differential levelling for the geodetic tie.

Repeat differential levelling and InSAR are two different relative measurement techniques: levelling measures multiple short-distance (maximum of ~40 m sight length) height differences from ground-based instruments set up orthogonal to the local gravity vector (e.g., Vaníček et al. 1980), while InSAR measures the geometric off-nadir LoS using radar backscatter from the Earth's surface back to the satellite (see e.g., Hanssen 2001) from repeat orbits (e.g., 11 days for TSX). Hence, repeat levelling measures the height difference between specific points on land during separate surveys (ideally four times per year for VLM monitoring) with respect to the local gravity vector, but InSAR measures the changes in LoS range between the ground (over a 'pixel', not a specific point) and the satellite for multiple pixels within the scene (50 km x 30 km for TSX stripmap). The processed InSAR LoS ranges, and repeat levelling surveys produce displacement time series, but at different spatial and temporal resolution with their own specific measurement and error characteristics. Both time series can be used to estimate rates of VLM at tide gauges, relative to a cGPS station, as we demonstrate for InSAR.

Mahapatra et al. (2018) used a radio transponder co-located at a tide gauge in the Netherlands to determine InSAR VLM rates relative to the tide gauge and co-located cGPS. However, tide gauge co-located InSAR ground infrastructure, such as transponders and corner reflectors (CRs) are not available at most global tide gauges, all of which need

158 monitoring for VLM to estimate accurate rates of SLC. Indeed, Wöppelmann and Marcos
159 (2016) report that only 14% of the Global Sea Level Observing System (GLOSS) tide gauges
160 have co-located cGPS stations (i.e., fixed directly to the tide gauge structure), so that
161 differential VLM for the tide gauges where cGPS is not co-located will need to be monitored.
162 While the use of transponders and CRs may provide improved location accuracy (e.g.,
163 Mahapatra et al., 2014; Dheenathayalan et al. 2016; 2017; Garthwaite 2017), these are not
164 likely to be available on a global scale for some years, and perhaps never for countries that
165 cannot afford such infrastructure. Hence, we test differential InSAR to tide gauges as a test
166 for an alternative technique that could potentially be applied globally, depending on the
167 availability of SAR imagery.
168
169 **2. Methods and data**
170 The data used and processing methods described in this section are arranged with a sub-
171 section for each technique. The cGPS in the test site (International GNSS Service (IGS) code
172 PERT; Figure 1), is used to transform the InSAR displacement time series to a terrestrial
173 reference frame (TRF) – IGS08 for this experiment – which is aligned with the International
174 reference Frame 2008 (ITRF2008; Altamimi et al. 2011). Derived TSX IGS08 rates can then
175 be compared to cGPS IGS08 rates at other locations for validation, and the TSX rates at each
176 tide gauge are then in a known TRF.
177 We use PERT as the single reference point because it is considered the most reliable
178 site for (1) cGPS time series (since 1995) and (2) the TSX reference pixel close to the cGPS.
179 This is compared to HIL1 which is co-located with HILS on the roof of the tide gauges shed
180 on a jetty in a boat harbour full of moored yachts with tall masts, and CUAI which is
181 mounted atop a 4-story building.
182 ***2.1 InSAR***

We first processed the 141 TSX scenes using the small baseline multi-temporal InSAR (MTI) method implemented in the Stanford Method of Persistent Scatterer (StaMPS; Hooper et al. 2012) software as described in Hooper (2008). The interferograms were processed using Doris (Delft object-oriented radar interferometric software; Kampes and Usai 1999), forming 705 small baseline interferograms. The small baselines interferogram pairs were selected manually, with the objective of keeping perpendicular (i.e., the distance between repeat satellite positions, orthogonal to the LoS) and temporal baselines as small as possible, but retaining redundancy in the network so that each scene was connected by at least three small baseline interferograms.

The high redundancy small baselines help reduce the effect of temporally variable tropospheric noise (Williams 1998; Agram and Simons 2015; Fattahi and Amelung 2015; Cao et al. 2018), which was also accounted for in the time series analysis in section 3.2. The phase ramp was estimated and used to remove the long-wavelength orbit and ionosphere effects that may be present in the TSX scene extent of 50 km x 30 km. This is appropriate for extents of <100 km (Hooper et al. 2012), but also because X-band is less affected by the ionosphere (cf. Gomba et al. 2017), TSX orbit errors are relatively small (Fattahi and Amelung 2014), and the study area is relatively flat, so less affected by stratified tropospheric effects (Bekaert et al. 2015).

The TSX slowly-decorrelating filtered phase (SDFP; Hooper 2008) pixels (stripmap spatial resolution ~3 m) were down-sampled to 30 m spatial resolution, using the method of Hooper et al. (2012), resulting in 827,215 points. The pixels were down-sampled to reduce the computing load and smooth noisy pixels, and were calculated using nearby pixels weighted from their signal-to-noise ratio (Hooper et al. 2012). Earlier experiments with the individual TSX SDFP pixels for the 4-year 2012.7-2016.7 time series (10,175,104 versus 728,702 down-sampled pixels) indicated that the rates from the down-sampled pixels were

more reliable when tested with independent results (i.e., cGPS and altimetry minus tide gauge VLM rates). For this reason, the down-sampled pixels were used in this experiment, and referred to herein as DPs. The TSX phase differences were unwrapped using 3D phase unwrapping (Hooper et al. 2007), and initially relate to an arbitrary datum where the mean of all velocities is taken as the zero reference.

The small baseline $m\ x\ n$ array comprises unwrapped DP phase differences ($\Delta\phi$), where m is the number of DPs (827,215) and n is the number of small baseline interferograms (705). To compute relative displacements for each DP per scene acquisition (t_a), which is 140 for this time series (first column of 141 scenes is removed; see below), a coefficient matrix **G** (n x p) is formed that describes the functional relation between the small baseline interferograms and the number (p) of t_a (705 x 140). The vector of phase displacements $\boldsymbol{d}$ for each DP is computed row by row, where $\Delta\boldsymbol{\phi} = \boldsymbol{G}\boldsymbol{d}$ using Gaussian elimination to invert the matrix. Each successive computation of $\boldsymbol{d}$ builds the $m\ x\ p$ displacement matrix $\boldsymbol{D}$. To remove the rank defect from **G**, the first column is removed (leaving 140 from 141 scenes) so that the first acquisition becomes t_0 and is the zero reference for the time series of displacements. This means that the TSX time series displacements will be relative to zero, so that although the displacement trends are transformed relative to the IGS08 reference frame, TSX DPs do not become IGS08 heights. The $\boldsymbol{D}_{\boldsymbol{m,p}}$ (827,215 x 140) displacement array is later transformed to the TRF (section 2.5).

2.2 GPS

Daily cGPS positions were obtained from the Nevada Geodetic Laboratory (NGL; http://geodesy.unr.edu/NGLStationPages/GlobalStationList; Blewitt et al. 2018). These data were used to estimate time series velocities using the CATS software (Williams 2008). The spectral index was solved for the five-year TSX period (2012.8-2017.8) using 11 cGPS

receivers located on buildings in addition to PERT (pillar mounted) and HIL1 (co-located with HILS). The average spectral index was –0.72 for all 11 cGPS time series, so this was used to recompute the trend with the annual and semi-annual terms and variable white noise. This was done to avoid introducing a bias in the spectral indices at PERT, HIL1 or CUAI that could have resulted from the shorter and variable time series. Only one of these building-mounted cGPS (CUAI; Figure 1) was used to provide an additional cGPS comparison for the TSX, because many are fixed to the same building, while several other time series were incomplete for the full TSX time period.

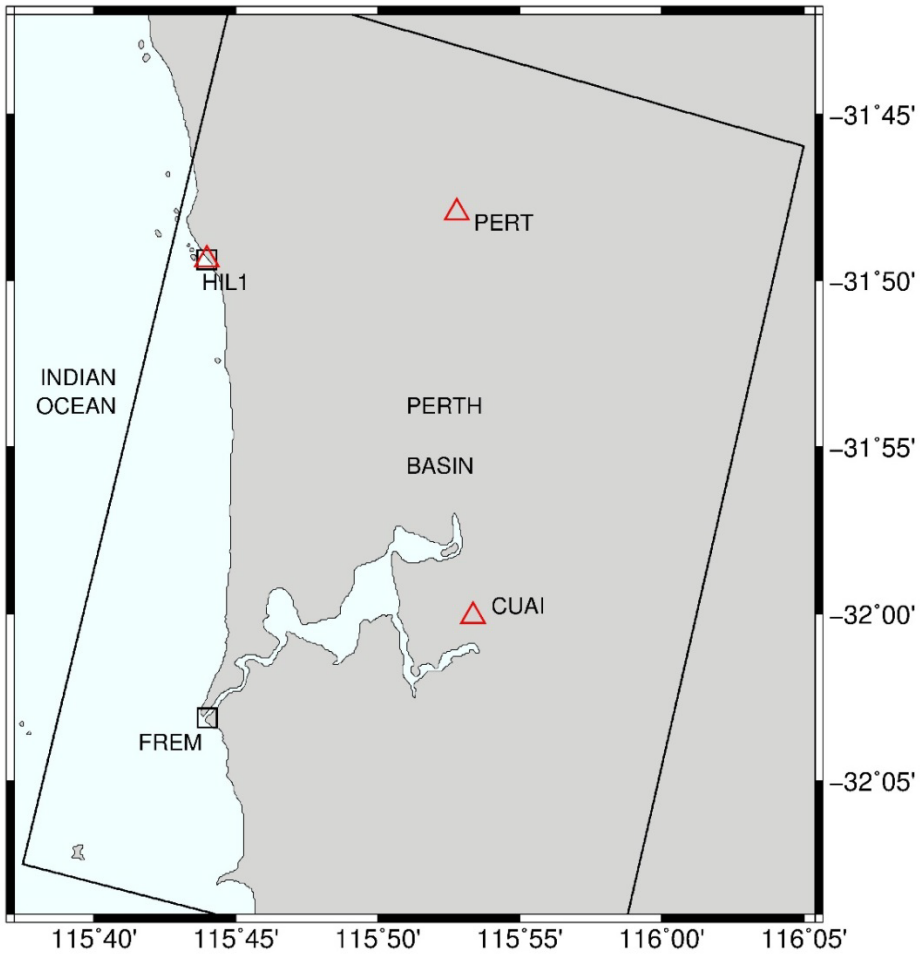

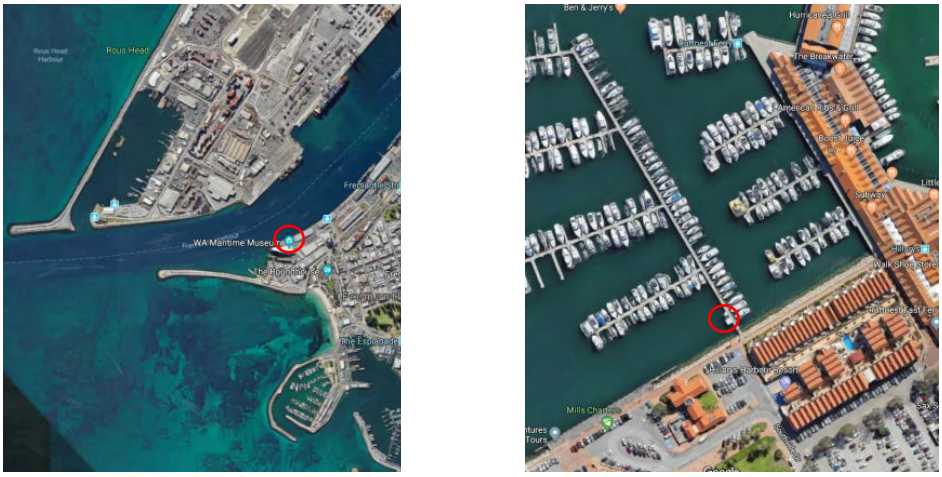

Figure 1: (Top) Map showing the test site, with cGPS stations (red triangles) and tide gauges (black squares), with the extent of the TSX scene shown by the black line. cGPS CUAI is located on top of a multi-storey building. (Bottom) FREM tide gauge (centre), and HIL1 co-located cGPS and HILS tide gauge (right) are shown in the red circles. Bottom images sourced from Google Earth.

2.3 Tide gauge sea level

Monthly mean sea level values from the Permanent Service for Mean Sea Level (PSMSL, Holgate et al 2013) were used for 1993.0–2018.0 (altimeter period) and for 2012.8–2017.8 (TSX period) to compare InSAR VLM rates to (1) tide gauge minus altimetry VLM at HILS and FREM, and (2) to differential tide gauge minus altimetry VLM rates between these gauges. HILS and FREM are ~30 km apart (Figure 1), where any difference in SLC is assumed to be due to relative tide gauge VLM (e.g., Burgette et al. 2013), so this will be used to provide some additional evidence to support the TSX differential VLM (but not absolute VLM in the IGS08 TRF). In creating the gridded altimeter product, a dynamic atmosphere correction has been applied by AVISO. This accounts for the inverse barometer effect at all periods, and for barotropic ocean dynamics at periods shorter than 20 days. For consistency, the same correction was applied to each of the tide gauge time series, as extracted from the

nearest grid point of the ocean model output. The effect of long period tides (Woodworth, 2012) was found to be below 0.03 mm/yr and was thus neglected.

The CATS software was first used to estimate rates and uncertainties for the full sea level records at both tide gauges as a check on the results and data. The power law index was –0.96 for the full (>100 year) FREM record, indicating flicker noise. Similar results were obtained for HILS, with a power law index of –1.14 for the full (~25 year) record. To avoid a possible bias in the sea level rates from using a spectral index computed from a short period time series, , the five-year rates were recomputed in CATS with the power law index fixed at –0.96 (see Table 2 later), on the assumption that the true spectral index of two tide gauges close together should be very similar.

2.4 Altimetry sea level

To compare the InSAR-derived VLM, tide gauge sea level observations minus satellite altimetry observations near the tide gauge can be used to estimate VLM at the tide gauge (e.g., Pfeffer and Allemand 2016; Wöppelmann and Marcos 2016, and many others). Altimetry data from AVISO (the Ssalto/Duacs, delayed mode, gridded absolute dynamic topography product using all available satellites, and with a dynamic atmosphere correction applied as described above) was used to estimate monthly sea surface heights adjacent to the two tide gauges. Data were extracted from the grid point within 200 km of the tide gauge which explained most of the variability seen at the gauge. This is a compromise, designed to limit the effect of increased instrumental and sampling errors near the coast, balanced against the inevitable loss of some near-coastal signal, and inevitable (and time dependent, as the satellite systems evolve over time) limitation of the satellite measurement system. Tide gauge sea level monthly means were subtracted from altimetry monthly means with the VLM rates estimated using CATS from the differenced time series for the full altimeter record (1993.0-

2018.0) and for the TSX period (2012.8-2017.8), after accounting for annual and semi-annual terms. This method assumes that, apart from any seasonal cycle, altimetry sea level realises the 'true' SLC rate at the tide gauge, with the difference to tide gauge sea level interpreted as the VLM at the tide gauge, with other errors (e.g., altimetry observation and processing errors) assumed negligible. Wöppelmann and Marcos (2016) estimated global tide gauge minus satellite altimetry uncertainties of up to ±3 mm/yr, but with a median of ±1 mm/yr from a set of 478 selected global tide gauges.

2.5 Transformation of InSAR time series to TRF

Transforming the TSX LoS rates into a TRF is important so that the rates from different measurement techniques (i.e., GPS, InSAR and altimetry) can be directly compared (cf. Wöppelmann et al. 2007; Bekaert et al. 2017; Hammond et al. 2018; Mahapatra et al. 2018). Using the S-transform method from Mahapatra et al. (2018) for a large data set, the **I** matrix (m x m) becomes large, and we found the m = 827,215 array to be beyond available computer memory. An alternative method was therefore implemented, where the TSX reference point (RP) displacement row vector $\mathbf{d}_{RP}$ is subtracted from all $\mathbf{d}_i$, (DP displacement vectors held in the displacement matrix **D**) where $\mathbf{d}_{RP}$ is given a (temporary) arbitrary zero displacement for all acquisition times (t_a). This produces the same results as the S-transform method but is done as a direct operation on **D** and does not require the computation of the large **I**.

The $\mathbf{d}_i$ are then transformed to the TRF through the connection between $\mathbf{d}_{RP}$ and the cGPS time series, which are treated as co-located (cf. Figure 2A). The velocity is computed from the cGPS time series (Section 2.2) for the same period as the InSAR $\mathbf{d}_{DP}$ (2012.8-2017.8) so that the $\mathbf{d}_i$ time series transformed as (Mahapatra et al. 2018)

$$\mathbf{d}_{i,TRF} = \mathbf{d}_i + \mathbf{H}\mathbf{d}_{GPS} \quad (1)$$

where $\mathbf{d}_{i,TRF}$ is $\mathbf{d}_i$ related to the TRF. **H** is a vector constraint to set the datum of a free network (here comprising ones whereby the average of all displacements is taken as the reference) and $\mathbf{d}_{GPS}$ is the vector of linear displacements at each TSX t_a from the estimated cGPS trend connecting the InSAR DPs to the TRF computed as

$$\mathbf{d}_{GPS} = v_{GPS} \times (t_a - t_0)/365.25 \quad (2)$$

where v_{GPS} is the estimated linear velocity of the cGPS time series in mm/yr and $(t_a - t_0)$ is the period (days) over which v_{GPS} is computed, then converted to years by dividing by 365.25. The resulting displacement array $\mathbf{D}_{TRF}$ comprises row vectors $\mathbf{d}_{i,TRF}$ representing each DP displacement transformed into the TRF. The TSX rate and uncertainty can then be computed from $\mathbf{d}_{i,TRF}$ at the tide gauge locations.

3. Results and Discussion

3.1 Time series comparisons

Initial comparisons were made between the cGPS and TSX time series as a check. Figure 2 shows the cGPS time series at PERT, HIL1 and CUAI compared to their nearest TSX DP before and after transformation to IGS08 constrained to the CATS-estimated cGPS IGS08 rate at the RP (PERT). The linear rate (red dots in Figure 2A) presents the transformed TSX rate, which is now coincident with the cGPS rate. The pre-transformation TSX time series (green triangles) indicates that it is sensing similar VLM signals to the cGPS. The main differences are between the maximum amplitude of the cGPS annual periodic signal, where the TSX amplitudes are, generally lesser magnitude. This may be due to the different measurement and processing characteristics of the SAR and GPS systems. For instance, the TSX may be sensing a close-by, but different, feature to the cGPS structure, and also the filtering in the TSX processing may tend to over-smooth the seasonal amplitude when compared with the higher solution rate of the cGPS.

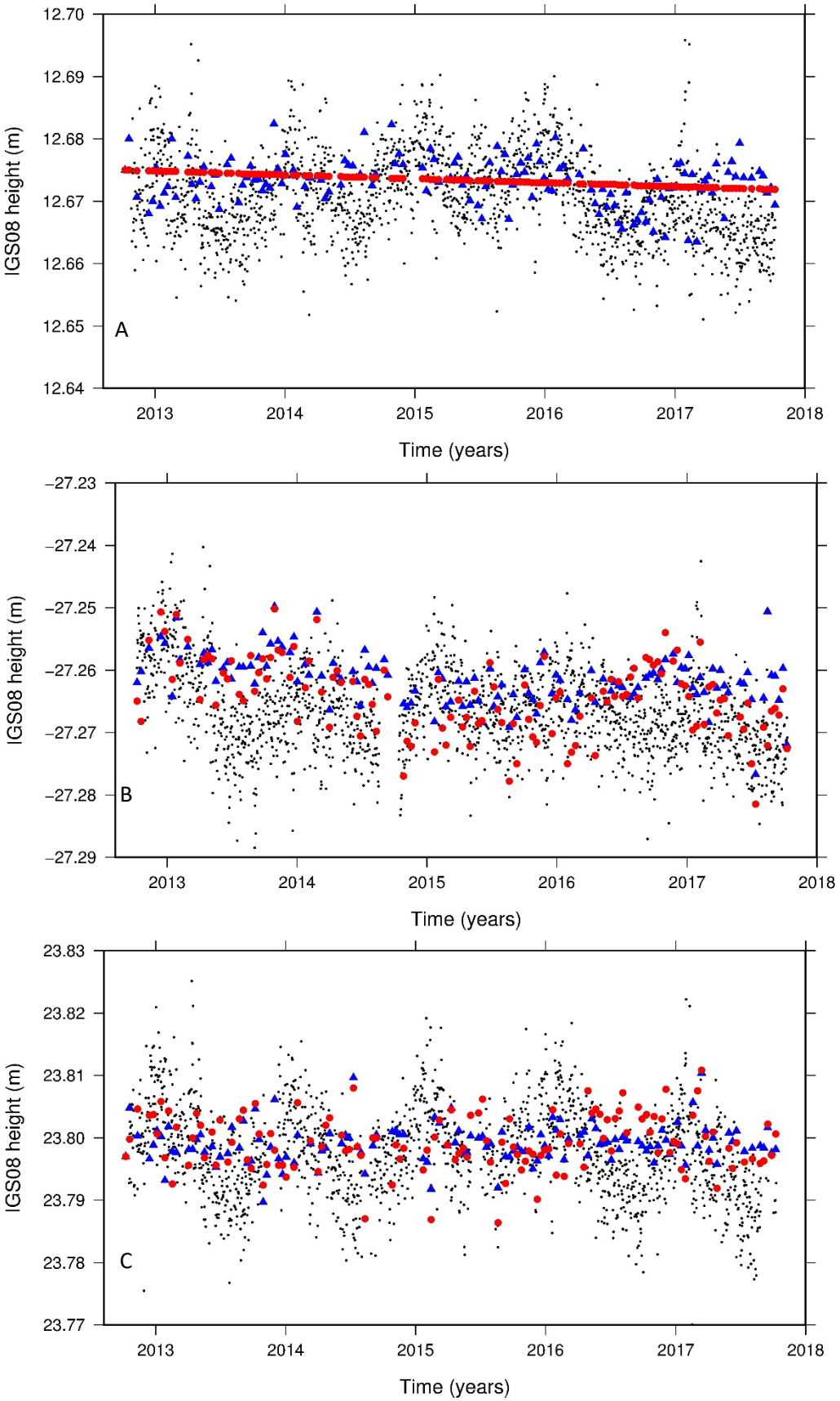

Figure 2: (A) PERT cGPS (IGS08) time series (black dots) compared to the time series for the nearest TSX LoS DP before transformation (blue triangles) and after transformation (red

circles). (B) As for (A), but for HIL1 cGPS time series and nearest TSX LoS DP before and after the rates have been transformed; (C) As for (B), but for CUAI cGPS time series and nearest TSX LoS DP. Note that the cGPS time series daily solutions are IGS08 heights, but the TSX time series displacements are relative to zero, shifted on the y-axis to IGS08 heights for plotting purposes to compare to the cGPS time series.

Both the TSX and GPS time series in Figure 2A suggest an uplift trend until 2016, and then appear to subside after this, although this should be viewed cautiously for a relatively short time series, and in the presence of the GPS seasonal signal. The HILS TSX and HIL1 GPS time series in Figure 2B do not agree as well as at PERT, although there are still similarities between them. HIL1 is a 'noisier' site than PERT, for both GPS and the TSX because of the masts on yachts moored nearby, and also because the TSX may not be sensing the tide gauge location exactly (cf. Figure 1). Similar problems may be experienced at some global tide gauges where this method may be applied.

The rate for a cGPS station located on top of a multi-storey building at Curtin University (Figure 1C) was also estimated as an additional comparison on the TSX. Although a site on a building is not ideal due to building movement (e.g., thermal expansion and contraction), and because the TSX DP may not sense the same position on the building, it was used only as a check for the TSX VLM rates.

3.2 InSAR noise analysis

To estimate the uncertainty of the InSAR trends, an analysis of the correlated noise in this time series was conducted (cf. Williams et al. 1998; Williams 2003; 2008). The relatively short time series of five years and 141 epochs limits the maximum likelihood estimation (MLE) of power-law and white noise, so only the power-law model was used. In this

approach, all 827,215 DPs in the SAR scene were included in the noise estimation on the assumption that the TSX time series noise is the same across the scene, and that the mean of the noise estimates for each DP would provide a more robust estimate of the spectral index. To reduce the computational burden, a single covariance matrix was precomputed and applied to all 827,215 DP time series in the image. A log-likelihood (LL) calculation was run on a range of spectral indices from –2 (random walk) to +1 (at 0.1 intervals) for all DP time series to find the maximum LL (Figure 3A) and then interpolate the MLE to get the best estimate of the spectral index for all DP time series.

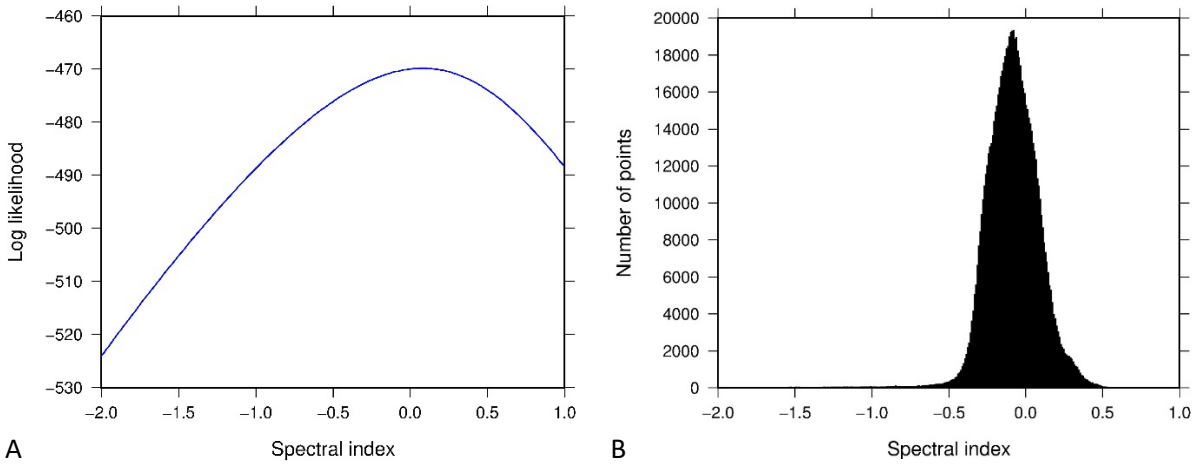

Figure 3: (A) is the log-likelihood (LL) for TSX DP #1 as a function of spectral index. The estimated spectral index is calculated from the largest LL and the two values either side. (B) Histogram of spectral indices for each transformed TSX DP time series.

Simulated Spectral Index	Estimated Spectral Index
0.00	0.19 ± 0.19
-0.09	0.10 ± 0.18
-0.26	-0.08 ± 0.18
-0.50	-0.33 ± 0.18
-1.00	-0.85 ± 0.17

Table 1: Simulated fixed spectral index and spectral index estimated as the standard deviation of all DP time series in the TSX data.

The spectral indices of all 827,215 DP time series is shown in Figure 3, with a mean value of –0.09. The estimated spectral index from this five-year time series may be biased on the low side because we remove a very large component of the correlated signal when the slope is estimated, some of which may contain coloured noise. To test the possible bias, we simulated noise with a fixed spectral index and the same number of points in the TSX data, then estimated the spectral index. The test indicates the true spectral index from the data is likely to be higher (more negative) than that estimated and shown in Table 1. The range (highest to lowest) of the simulated estimates is similar to those computed from the data (~1.0), so from Table 1 we adopt the estimated spectral index value of –0.08 (closest to the computed value of –0.09) which is then related to the corresponding simulated spectral index of –0.26.

3.3 Sea level rates

Linear rates of SLC from the tide gauges and altimetry for 1993.0-2018.0 and for the TSX period 2012.8-2017.8 are shown in Table 2. The 1993.0-2018.0 SLC rates are included as a comparison, with the shorter period being more affected by variability in short term sea level (Woodworth et al. 2019). The short-term relative sea level rates are of less interest in this study, but the differential rates between the tide gauge sites are used to support the validity of the TSX VLM (Section 3.4). The tide gauge rates comprise VLM that is dependent on the tide gauge site, and also the sea level signal. The altimetry measures only sea level at a location offshore from the tide gauge. Over a distance of only ~30 km, the sea level rate should be the same, as seen by the altimetry over the longer 1993.0 – 2018.0 period, so that the differential rate between the tide gauges is assumed to be primarily VLM. The tide gauge differential rate sums to ~47 mm over 25 years, which compares to ~70 mm over 40 years in Featherstone et al. (2015) from repeat levelling.

	SLC 1993.0-2018.0 (mm/yr)	SLC 2012.8-2017.8 (mm/yr)
FREM		
Tide gauge	+6.95±2.66	-11.90±9.67
Altimetry	+5.23±2.47	-14.52±9.77
HILS		
Tide gauge	+8.84±2.58	-13.96±10.04
Altimetry	+5.29±2.51	-18.49±9.48

Table 2: Tide gauge and altimetry sea level rates for FREM and HILS. The tide gauge rates contain the VLM and the ocean signal, whereas the altimetry contains only the sea level rate.

All VLM rates were computed using CATS, as described in Sections 2.2, 2.3 and 3.2. The tide gauge minus altimetry VLM rates were estimated from the differenced monthly means (as per Section 2.4) so are slightly different to the differences of the rates shown here. The differential tide gauge minus altimetry VLM rate between the tide gauges was also estimated from the double differences of the tide gauge and altimetry monthly means, which resulted in reduced uncertainties to those shown in Table 2. Double differencing was used only for the tide gauge and altimetry sea level measurements because the ocean contains large annual, interannual and decadal variabilities to which linear rates can be more sensitive than GPS and TSX

3.4 VLM rates

The small baseline LoS phase differences were converted to VLM displacements for each DP on the assumption that there is no relative horizontal motion among the cGPS and tide gauges (indicated to be the case for this test site in Parker et al. 2017). All DP time series displacements were then referenced to the TRF at the cGPS (PERT) using the methods described in Section 2.5. Equations (1) and (2) were used to transform to the TRF through the

connection to the cGPS, using v_{GPS} = –0.62±0.51 mm/yr for PERT in the TRF. This cGPS rate was estimated using CATS for 2012.7-2017.7 as per Section 2.2.

The TSX rates were computed in CATS using the fixed spectral index of –0.26 estimated in Section 3.2, variable white noise and annual and semi-annual terms. These rates are shown in Figure 4, with Figure 4A showing DPs close to the cGPS (RP used is calculated within 4 m) with rates between –0.5 mm/yr and –1.0 mm/yr (RP fixed to –0.62 mm/yr). This indicates that the land surrounding the cGPS is subsiding at a similar rate to the cGPS structure so that it is reasonable to adopt the closest DP as TSX RP in this case.

Figure 4B shows the region adjacent to FREM to be uplifting in the range +0.5 mm/yr to +1.0 mm/yr, but the location of the tide gauge itself is in the 0.0 mm/yr to +0.5 mm/yr range (FREM +0.45 mm/yr). The area showing the higher uplift is covered by several buildings, so these may be the dominant scatterers near this location. The subsidence experienced by the coastal breakwater structure to the north of FREM is notable, as is the area along the waterfront to the south. These comprise human-made structures that are liable to settlement and subsidence. The areas without DPs are likely due to temporal decorrelation, from vegetation changes or in the car parks and vehicle unloading/storage area on the docks where the position and cars will not be the same for each SAR acquisition. The VLM in the vicinity of Fremantle is variable, ranging from +2 mm/yr to <-3 mm/yr which reinforces the need to monitor VLM at the tide gauge site, rather than simply adopt the rates from a remote cGPS station that is not co-located with the tide gauge.

The DPs near HIL1 and HILS (Figure 4C) also indicates consistency in the –1 mm/yr to –1.5 mm/yr range (HIL1 TSX rate at –1.20 mm/yr), which supports the adoption of the nearest DP. It is not clear if the DP adopted is actually sensing the tide gauge itself or the close by land (within ~5 m), but they do appear to be subsiding at similar rates.

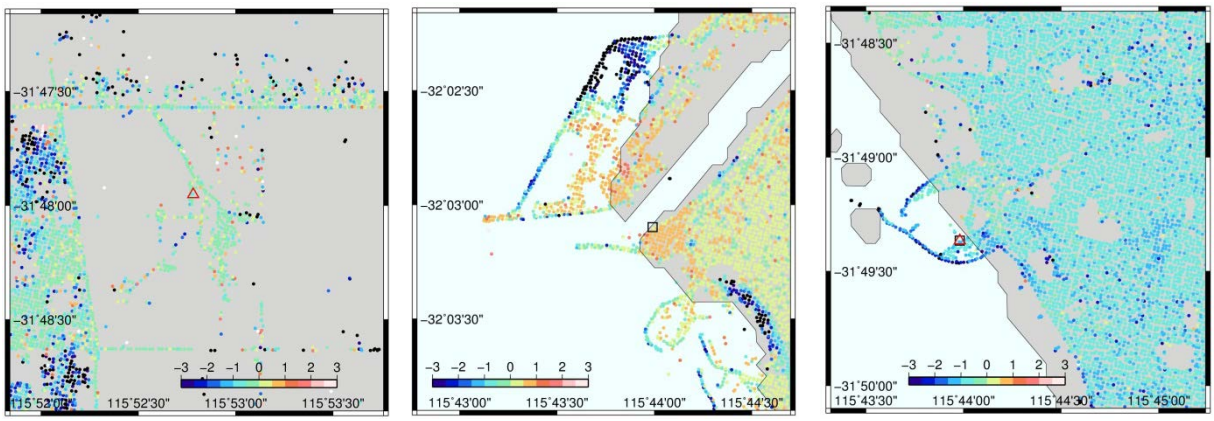

Figure 4: TSX DP rates (mm/yr) around (A) PERT (red triangle); (B) FREM (black square).; (C) HIL1 (red triangle), and co-located HILS tide gauge (black square).

The VLM rates from the different measurement techniques are summarised in Figure 5, and listed in Table 3. The difference between the 2012.8-2017.8 cGPS rates (red triangles) and the TSX rates (green circles) at HIL1 (cGPS –1.94±0.53 mm/yr; TSX –1.20±0.40 mm/yr) and CUAI (cGPS –0.78±0.60 mm/yr; TSX –0.08±0.38 mm/yr) indicate the precision of the TSX within the TRF. Although the agreement is at the edge of the respective error bars (Figure 5), the differences are <0.74 mm/yr, so less than the median uncertainty of ±1 mm/yr for altimetry minus tide gauge VLM from the global study of Wöppelmann and Marcos (2016). The CATS-derived cGPS rates are both less than the CATS-derived TSX rates (larger subsidence for GPS), which indicates a bias, although this cannot be certain for only two cGPS stations, one of which is building-mounted. The TSX at FREM indicates small uplift of +0.45±0.40 mm/yr, which is barely significantly different from zero VLM (cf. Burgette et al. 2013), but this is inclusive to the 2012.8-2017.8 period only, and care should be taken in making direct comparisons with VLM rates from different periods, especially as some parts of the Perth Basin have experienced non-linear subsidence (Featherstone et al. 2015). Longer period cGPS rates are shown in Table 3 from the University of La Rochelle processing

(ULR6A, Santamaría-Gómez et al. 2017) and the Median Interannual Difference Adjusted for Skewness (MIDAS) method (Blewett et al. 2016). These are shown to provide an additional comparison for the longer term rates serving as a 'sanity' check for the other rates of similar periods, and also give an indication whether there is non-linearity at the VLM at these sites when compared to different periods.

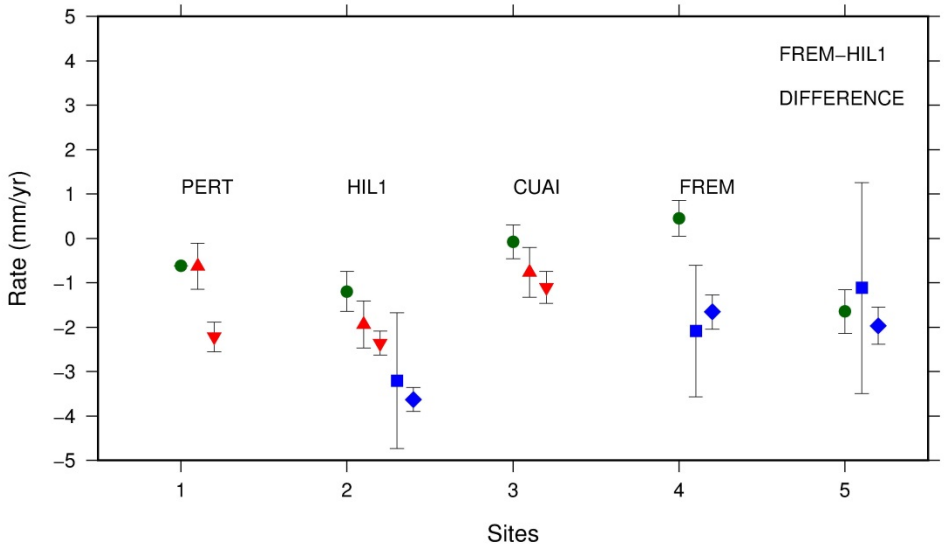

Figure 5: Velocity estimates (mm/yr) for TSX 2012.8-2017.8 (green circles), GPS 2012.8-2017.8 (red triangles); ~1996.0-2019.3 (inverted red triangles) and tide gauge minus altimetry VLM 2012.7-2017.7 (blue squares) and 1993.0-2018.0 (blue diamonds). So-called 'Site' 5 actually shows the differential VLM between HILS and FREM for TSX and tide gauge minus altimetry. See Table 3 for numerical VLM rates.

The tide gauge minus altimetry VLM rates for 2012.8-2017.8 are –2.09±1.48 mm/yr and –3.21±1.53 mm/yr (Table 3) for FREM and HILS, respectively, which appear to be systematically larger subsidence rates than the TSX (~2-2.5 mm/yr more subsidence), which is referenced to IGS08 at the PERT cGPS. These differences are statistically significant, and also larger than the ±1 mm/yr uncertainty estimate for tide gauge minus altimetry VLM from Wöppelmann and Marcos (2016), suggesting that the constant offset may be a systematic bias

493 between the IGS08-referenced TSX and the tide gauge minus altimetry VLM. The cGPS
494 rates at HIL1 and CUAI are closer to the TSX (~0.74 mm/yr) than the altimetry minus tide
495 gauge VLM at HILS (~1.2 mm/yr), suggesting that the TSX is slightly closer to the true
496 VLM rate, albeit on the assumption that cGPS is the most reliable technique for determining
497 VLM. In this comparison, the differential TSX is referenced to cGPS at PERT, so can be
498 directly compared to cGPS processed in the IGS08 reference frame.

Site	TSX 2012.8-2017.8	cGPS 2012.8-2017.8	Alt-tide gauge 2012.8-2017.8	Alt-tide gauge 1993.0-2018.0
PERT	–0.62±0.00(2)	–0.62±0.52		
HIL1/HILS	–1.20±0.45	–1.94±0.53	–3.21±1.53	–3.63±0.26
CUAI	–0.08±0.38	–0.78±0.60		
FREM	+0.45±0.40		–2.09±1.48	–1.66±0.38
HILS – FREM difference	–1.65±0.49		–1.12±2.38	–1.97±0.42

499
500 Table 3: Multi-technique VLM rates for each site (including HILS – FREM VLM
501 difference).

502

503 To investigate the possible non-linearity of VLM at these sites, we have shown
504 longer term (1993.0-2018.0) rates for altimetry minus tide gauge (Table 3) and cGPS VLM
505 (various periods; Table 4)., These are also plotted in Figure 5, and suggest that the rates
506 shown here are dependent on the time period used, suggesting non-linearity (cf. Burgette et
507 al. 2013; Merrifield and Thompson 2018). This is most evident at PERT, where the 2012.8-
508 2017.8 cGPS rate is –0.62±0.51 mm/yr (Table 3), but for 1996.0-2019.3 (Table 4) is –
509 2.22±0.33 mm/yr, which is in agreement with –2.09±0.38 (1995.0-2014.0) for ULR6
510 (Santamaria-Gomez et al. 2017) and –2.34±0.59 (1996.0-2019.3) for MIDAS (Blewitt et al.
511 2016). Non-linearity is less obvious at HIL1 (–1.94±0.53 mm/yr compared to –2.36±0.27
512 mm/yr for 1996.0-2019.3), although this location has been shown by Featherstone et al.
513 (2015) to have undergone non-linear subsidence due to increased groundwater extraction in
514 the early 2000s. HIL1 cGPS rates from ULR6 (Santamaria-Gomez et al. 2017) are –

515 2.78±0.31 mm/yr (2005.0-2014.0) and from MIDAS (Blewitt et al. 2016) are –2.69±0.62
516 mm/yr (1997.7-2019.3

Site	cGPS
PERT (NGL) 1996.0-2019.3	–2.22±0.33
PERT (ULR6) 1995.0-2014.0	–2.09±0.38
PERT (MIDAS) 1996.0-2019.3	–2.34±0.59
HIL1/HILS (NGL)1996.0-2019.3	–2.36±0.27
HIL1 (ULR6) 2005.0-2014.0	–2.78±0.31
HIL1 (MIDAS) 1997.7-2019.3	–2.69±0.62

517

518 Table 4: Longer period rates for cGPS stations from NGL time series processed for this study
519 in CATS, ULR6 (Santamaría-Gómez et al. 2017) and MIDAS (Blewett et al. 2016) (ULR6
520 and MIDAS rates and time period from SONEL, see text for URL).

521

522 The tide gauge minus altimetry VLM for the TSX period is not statistically different
523 to the 1993.0-2018.0 period, although this is partly due to the larger uncertainty in the TSX-
524 period VLM. The difference between long-term HIL1 (–2.36±0.27 mm/yr) and HILS tide
525 gauge minus altimetry (–3.63±0.26 mm/yr) VLM is statistically significant, and although
526 over slightly different periods (1996.0-2019.3 and 1993.0-2018.0 respectively) suggests a
527 bias between these techniques at the two tide gauges.

528 The difference between the two tide gauge's VLM from the InSAR and tide gauge
529 minus altimetry as shown on the right-hand-side ('site' 5) of Figure 5 is important. The close
530 proximity of these two sites (~30 km) allows the comparison of the differential VLM from
531 these two independent techniques, and it indicates that they produce similar results, at least
532 for this experiment. It suggests that while there may be offsets in one (or both) of these
533 techniques, the differential VLM from each is in good agreement.

534

535 **4. Conclusion**

Differential VLM rates from TSX appear to deliver similar precision to that estimated from first order differential levelling in the study of Lyon et al. (2018; both around ±0.4 mm/yr to ±0.5 mm/yr), although this is dependent on the time period and number of observations in each. Differential TSX rates give a good agreement with tide gauge minus altimetry differential VLM between the two tide gauges. When comparisons are made for the 2012.8 – 2018.8 period between VLM rates from TSX referenced to IGS08 at PERT, altimetry minus tide gauge and cGPS rates in IGS08, there appear to be systematic offsets. It is not yet clear if this is the limit of the techniques' precision, the result of systematic differences between the techniques, or their accuracy within their respective reference frames over this shorter time period.

TSX VLM at FREM referenced to IGS08 at PERT cGPS is +0.45±0.40 mm/yr for 2012.8-2017.8. This slight uplift is different to long-term subsidence rates of -1.66 mm/yr from tide gauge minus altimetry for 1993-2018, suggesting non-linear VLM at FREM, although this should be viewed cautiously considering the possibility of a systematic bias of up to 1 mm/yr in the tide gauge minus altimetry VLM rate.

These InSAR results suggest that when longer time series are established over more tide gauges, InSAR may provide remotely sensed estimates of differential VLM for tide gauge 'geodetic ties' that could be extended globally. The need for geodetic ties for global tide gauges to support sea level studies is made by Woodworth et al (2017, and others), so that the continued acquisition of long InSAR time series over tide gauges is of high importance to facilitate more detailed tide gauge VLM analyses in the future.

Acknowledgments

We would like to thank the following organisations for providing and/or funding these data. TerraSAR-X scenes are acquired under the German Space Agency's (DLR's) Science Project

561 LAN1499, funded by AuScope under the Australian Geophysical Observing System
562 (AGOS), and Australian Research Council (ARC) Linkage Projects LP 110100284 and
563 LP140100155. The Ssalto/Duacs altimeter products were produced and distributed by the
564 Copernicus Marine and Environment Monitoring Service (CMEMS)
565 (http://www.marine.copernicus.eu). Dynamic atmospheric Corrections are produced by CLS
566 using the Mog2D model from Legos and distributed by Aviso+, with support from CNES
567 (https://www.aviso.altimetry.fr/). GPS data was obtained from Nevada Geodetic Laboratory
568 at http://geodesy.unr.edu/. Monthly sea level means were obtained from the Permanent
569 Service for Mean Sea Level (PSMSL) https://www.psmsl.org/. We would also like to thank
570 Professor Andy Hooper for making StaMPS software freely available and the Delft
571 University of Technology for providing the Doris software. Figures 1-5 were plotted using
572 the Generic Mapping Tools (Wessel et al. 2013; EOS 94(45):409–410,
573 https://doi.org/10.1002/2013EO450001)

574

575

576 **Data availability**

577 The TerraSAR-X scenes are available to us under licence through DLR Science Project
578 LAN1499, so cannot be made publically available.
579 ULR6 and NGL rates obtained from SONEL
580 (https://www.sonel.org/spip.php?page=gps&idStation=812&solCentre=ULR). Processed
581 GPS data are freely available at Nevada Geodetic Laboratory http://geodesy.unr.edu/, and
582 also SONEL https://www.sonel.org/-ULR-112-.html.
583 Monthly sea level records are freely available at PSMSL https://www.psmsl.org/.
584 Altimetry data is available at CMEMS http://www.marine.copernicus.eu

585 Dynamic atmospheric corrections (DAC) are available from Aviso+ at

586 https://www.aviso.altimetry.fr/

587

588 **References**

589 Adamska LM (2012) Use of persistent scatterer interferometry for the enhancement of vertical land movement
590 measurement at tide gauges around the British coast. PhD thesis, University of Nottingham, UK.

591 Agram PS, Simons M (2015) A noise model for InSAR time series. *Journal of Geophysical Research: Solid*
592 *Earth*, 120(4):2752-2771, doi:10.1002/2014JB011271.

593 Altamimi Z, Collilieux X, Metivier L (2011) ITRF2008: An improved solution of the International Terrestrial
594 Reference Frame. *Journal of Geodesy*, 85(5): 457–473, doi:10.1007/s00190-011-0444-4.

595 Bekaert DPS, Hooper A, Wright TJ (2015) A spatially variable power-law tropospheric correction technique for
596 InSAR data. *Journal of Geophysical Research: Solid Earth*, 120(2):1345–1356, doi:10.1002/2014JB011558.

597 Bekaert DPS, Hamlington BD, Buzzanga B, Jones CE (2017) Spaceborne synthetic aperture radar survey of
598 subsidence in Hampton Roads, Virginia (USA). *Science Reports*, 7: 14752, doi:10.1038/s41598-017-15309-
599 5.

600 Bevis M, Scherer W, Merrifield M (2002) Technical issues and recommendations related to the installation of
601 continuous GPS stations at tide gauges. *Marine Geodesy*, 25(1-2): 87–99,
602 doi:10.1080/014904102753516750.

603 Blewitt G, Kreemer C, Hammond WC, Gazeaux J (2016) MIDAS robust trend estimator for accurate GPS
604 station velocities without step detection. *Journal of Geophysical Research: Solid Earth*, 121(3): 2054-2068,
605 doi:10.1002/2015JB012552.

606 Blewitt G, Hammond WC, Kreemer C (2018) Harnessing the GPS data explosion for interdisciplinary science,
607 *EOS – Transactions of the American Geophysical Union*, 99, doi: 10.1029/2018EO104623.

608 Brooks BA, Merrifield MA, Foster J, Werner CL, Gomez F, Bevis M, Gill S (2007) Space geodetic
609 determination of spatial variability in relative sea level change, Los Angeles basin. *Geophysical Research*
610 *Letters*, 34(1), L01611, doi:10.1029/2006GL028171.

611 Burgette R, Watson CS, Church JA, Tregoning P, Coleman R (2013), Characterizing and minimizing the effects
612 of noise in tide gauge time series: Relative and geocentric sea level rise around Australia, *Geophysical*
613 *Journal of International*, 194(2): 719–736, doi:10.1093/gji/ggt131.

614 Cao·Y, Li Z, Wei·J, Hu J, Duan M, Feng G (2018) Stochastic modeling for time series InSAR: with emphasis
615 on atmospheric effects. *Journal of Geodesy*, 92(2):185–204, doi.org/10.1007/s00190-017-1055-5

616 Dheenathayalan P, Small D, Schubert A, Hanssen RF (2016) High-precision positioning of radar scatterer.
617 *Journal of Geodesy*, 90(5): 403-422, doi: 10.1007/s00190-015-0883-4.

618 Dheenathayalan P, Cuenca MC, Hoogeboom P, Hanssen RF (2017) Small reflectors for ground motion
619 monitoring with InSAR. *IEEE Transactions on Geoscience and Remote Sensing*, 55(12): 6703-6712, doi:
620 10.1109/TGRS.2017.2731424.

621 Fattahi H, Amelung F (2014) InSAR uncertainty due to orbital errors. *Geophysical Journal International*,
622 199(1)**,** 549–560, doi: 10.1093/gji/ggu276.

623 Fattahi H, Amelung F (2015) InSAR bias and uncertainty due to systematic and stochastic tropospheric delay.
624 *Journal of Geophysical Research: Solid Earth*, 120(12):8758-8773, doi:10.1002/2015JB012419.

625 Featherstone WE, Penna NT, Filmer MS, Williams SDP (2015) Nonlinear subsidence at Fremantle, a long-
626 recording tide gauge in the Southern Hemisphere. *Journal of Geophysical Research: Oceans* 120(10): 7004-
627 7014, doi: 10.1002/2015JC011295.

628 Ferretti A, Prati C, Rocca F (2001) Permanent scatterers in SAR Interferometry. *IEEE Transactions on*
629 *Geoscience and Remote Sensing*, 39(1): 8-20, doi: 10.1109/36.898661

630 Fielding EJ, Blom RG, Goldstein RM (1998) Rapid subsidence over oil fields measured by SAR interferometry.
631 *Geophysical Research Letters*, 25(17): 3215-3218, doi: 10.1029/98GL52260

632 Garthwaite M (2017) On the design of radar corner reflectors for deformation monitoring in multi-frequency
633 InSAR. *Remote Sensing*, 9(7): 648, doi:10.3390/rs9070648.

634 Hanssen RF (2001). *Radar Interferometry: Data Interpretation and ErrorAnalysis*, Kluwer, Academic.

635 Hamlington BD, Thompson P, Hammond WC, Blewitt G, Ray RD (2016) Assessing the impact of vertical land
636 motion on twentieth century global mean sea level estimates. *Journal of Geophysical Research Oceans*,
637 121(7): 4980–4993, doi: 10.1002/2016JC011747.

638 Hammond WC, Burgette RJ, Johnson KM, Blewitt G. (2018) Uplift of the Western Transverse Ranges and
639 Ventura Area of Southern California: A four-technique geodetic study combining GPS, InSAR, levelling,

640 and tide gauges *Journal of Geophysical Research - Solid Earth*, 123(1): 836–858, doi:
641 10.1002/2017JB014499.
642 Hooper A (2008) A multi-temporal InSAR method incorporating both persistent scatterer and small baseline
643 approaches. *Geophysical Research Letters*, 35(16):L16302, doi: 10.1029/2008GL034654.
644 Hooper A, Bekaert D, Spaans K, Arikan M (2012), Recent advances in SAR interferometry time series analysis
645 for measuring crustal deformation. *Tectonophysics*, 514–517: 1−13, doi:10.1016/j.tecto.2011.10.013.
646 Hooper A, Zebker HA (2007) Phase unwrapping in three dimensions with application to InSAR time series.
647 *Journal of the Optical Society of America A*, 24(9): 2737-2747, doi: 10.1364/JOSAA.24.002737.
648 Holgate SJ, Matthews A, Woodworth PL, Rickards LJ, Tamisiea ME, Bradshaw E, Foden PR, Gordon KM,
649 Jevrejeva S, Pugh J (2013) New data systems and products at the permanent service for mean sea level,
650 *Journal of Coastal Research*, 29(3), 493–504, doi:10.2112/JCOASTRES-D-12-00175.1.
651 Kampes B, Usai S (1999) Doris: The Delft object-oriented Radar Interferometric software. In: proceedings ITC
652 2nd ORS symposium, August.
653 King MA, Keshin M, Whitehouse PL, Thomas ID, Milne M, Riva RE (2012) Regional biases in absolute sea-
654 level estimates from tide gauge data due to residual unmodeled vertical land movement. *Geophysical*
655 *Research Letters*, 39(14), L14604, doi:10.1029/2012GL052348.
656 Kuo CY, Shum CK, Braun A, Mitrovica JX, (2004) Vertical crustal motion determined by satellite altimetry and
657 tide gauge data in Fennoscandia. *Geophysical Research Letters*, 31(1): L01608,
658 doi:10.1029/2003GL019106.
659 Le Cozannet G, Raucoules D, Wöppelmann G, de Michele M, Poupardin A (2014) InSAR monitoring of ground
660 motions impacts for in-situ sea level measurement: the example of Dakar (Senegal). IGARSS, Quebec City,
661 QC, Canada, 13-18 July 2014, doi: 10.1109/IGARSS.2014.6946588
662 Le Cozannet G, Raucoules D, Wöppelmann G, Garcin M, Da Sylva S, Meyssignac B, Gravelle M, Lavigne F
663 (2015) Vertical ground motion and historical sea-level records in Dakar (Senegal). *Environmental Research*
664 *Letters*, 10: 084016, doi: 10.1088/1748-9326/10/8/084016.
665 Lyon TJ, Filmer MS, Featherstone WE (2018) On the use of repeat leveling for the determination of vertical
666 land motion: artifacts, aliasing and extrapolation errors. *Journal of Geophysical Research: Solid Earth*,
667 123(8):7021-7039, doi: 10.1029/2018JB015705.

668 Mahapatra P, van der Marel H, van Leijen F, Samiei-Esfahany S, Klees R, Hanssen R (2018) InSAR datum
669 connection using GNSS-augmented radar transponders. *Journal of Geodesy*, 92(1):21–32,
670 doi:10.1007/s00190-017-1041-y.
671 Mahapatra P, Samiei-Esfahany S, van der Marel H, Hanssen R (2014) On the Use of Transponders as Coherent
672 Radar Targets for SAR Interferometry. *IEEE Transactions on Geoscience and Remote Sensing*, 52(3): 1869,
673 doi: 10.1109/TGRS.2013.2255881.
674 Mazzotti, S., C. Jones, and R. E. Thomson (2008) Relative and absolute sea level rise in western Canada and
675 northwestern United States from a combined tide gauge-GPS analysis. *Journal of Geophysical Research -*
676 *Oceans*, 113, C11019, doi:10.1029/2008JC004835.
677 Merrifield MA, Thompson PR (2018) Interdecadal sea level variations in the Pacific: Distinctions between the
678 tropics and extratropics. *Geophysical Research Letters*, 45(13):6604-6610, doi: 10.1029/2018GL077666
679 Parker AL, Filmer MS, Featherstone WE (2017) First results from Sentinel-1A InSAR over Australia:
680 Application to the Perth Basin. *Remote Sensing* 9(3): 299; doi: 10.3390/rs9030299.
681 Peltier WR (2004) Global glacial isostasy and the surface of the ice-age Earth: The ICE-5G (VM2) Model and
682 GRACE, *Annual Review of Earth and Planetary Sciences*, 32: 111-149, doi:
683 10.1146/annurev.earth.32.082503.144359.
684 Pfeffer J., Allemand P. (2016) The key role of vertical land motions in coastal sea level variations: A global
685 synthesis of multisatellite altimetry, tide gauge data and GPS measurements. *Earth and Planetary Science*
686 *Letters*, 439: 39-47, doi: 10.1016/j.epsl.2016.01.027.
687 Poitevin C, Wöppelmann G, Raucoules D, Le Cozannet G, Marcos M, Testut L (2019) Vertical land motion and
688 relative sea level changes along the coastline of Brest (France) from combined space-borne geodetic
689 methods *Remote Sensing of Environment*, 222: 275-285, doi:10.1016/j.rse.2018.12.035
690 Raucoules D, Le Cozannet G, Wöppelmann G, de Michele M, Gravelle M, Daag A, Marcos M (2013) High
691 nonlinear urban ground motion in Manila (Philippines) from 1993 to 2010 observed by DInSAR:
692 implications for sea-level measurements. *Remote Sensing of Environment*, 139:386-397,
693 doi:10.1016/j.rse.2013.08.021.
694 Rucci A, Ferretti A, Monti Guarnieri A, Rocca F (2012) Sentinel 1 SAR interferometry applications: The
695 outlook for sub millimeter measurements. *Remote Sensing of Environment*, 120:156-163, doi:
696 10.1016/j.rse.2011.09.030.
697 Santamaría-Gómez A, Gravelle M, Dangendorf S, Marcos M, Spada G, Wöppelmann G (2017) Uncertainty of

698 the 20th century sea-level rise due to vertical land motion errors, *Earth and Planetary Science Letters*, 473:
699 24–32, doi: 10.1016/j.epsl.2017.05.038.
700 Williams S, Bock Y, Fang P (1998) Integrated satellite interferometry: Tropospheric noise, GPS estimates and
701 implications for interferometric synthetic aperture radar products, *Journal of Geophysical Research –Solid*
702 *Earth*, 103(B11): 27,051–27,067, doi:10.1029/98JB02794.
703 Williams, SDP. (2008), CATS: GPS coordinate time series analysis software, *GPS Solutions*, 12(2), 147-153,
704 doi: 10.1007/s10291-007-0086-4.
705 Woodworth, P.L. (2012) A note on the nodal tide in sea level records. *Journal of Coastal Research,* 28 (2), 316-
706 323, doi: 10.2112/JCOASTRES-D-11A-00023.1
707 Woodworth, P.L., Wöppelmann, G., Marcos, M., Gravelle, M., Bingley, R.M. (2017) Why we must tie satellite
708 positioning to tide gauge data. *EOS – Transactions of the American Geophysical Union*, 98 (4): 13-15, doi:
709 10.1029/2017EO064037.
710 Woodworth, P.L., Melet A, Marcos M, Ray RD, Wöppelmann, G., Sasaki YN, Cirano M, Hibbert A, Huthnance
711 JM, Monserrat S, Merrifield MA (2019) Forcing factors affecting sea level changes at the coast. *Surveys in*
712 *Geophysics*, doi: 10.1007/s10712-019-09531-1.
713 Wöppelmann, G, Martin Miguez, B, Bouin, MN & Altamimi, Z (2007), Geocentric sea-level trend estimates
714 from GPS analyses at relevant tide gauges world-wide, *Global and Planetary Change*, 57(3-4), 396-406,
715 doi:10.1016/j.gloplacha.2007.02.002
716 Wöppelmann G, Le Cozannet G, De Michele M, Raucoules D, Cazenave A, Garcin M, Hanson S, Marcos M,
717 Santamaría-Gõmez,A (2013) Is land subsidence increasing the exposure to sea level rise in Alexandria,
718 Egypt? *Geophysical Research Letters*, 40 (12): 2953-2957, doi: 10.1002/grl.50568.
719 Wöppelmann G, Marcos M (2016) Vertical land motion as a key to understanding sea level change and
720 variability. *Reviews of Geophysics*, 54 (1): 64-92, doi: 10.1002/2015RG000502.
721